

Conditional Model-Adequacy Tests for Spectral Uncertainty Claims in Lattice QCD

Haozheng Li*

Center for High Energy Physics, Peking University, Beijing 100871, People's Republic of China

Euclidean lattice correlators determine spectral functions only through a smoothing integral transform, so a nominal uncertainty band on a reconstructed spectrum need not have a coverage interpretation for a physical summary. We formulate this as a target-wise adequacy test for reported spectral uncertainties. For a chosen summary $T[\rho]$, the reported interval is tested on Euclidean-admissible mock correlators with known truth using empirical coverage, simulation-based calibration ranks, physical diagnostics, and stress tests.

The test is conditional, but it is a useful falsification tool: passing it does not prove that a reconstruction is the QCD truth, while failing it shows that the reported uncertainty law is not adequate for the chosen functional under the stated mock extension. In a generic benchmark, peak locations are substantially better calibrated than peak heights or low-frequency weights, reflecting different degrees of functional identifiability under the Euclidean kernel.

We then apply the same logic to a finite-temperature shear correlator. A family of BG-style reconstructions is compatible with the Euclidean data at $\chi^2/N_\tau \simeq 1.3$. Within the scanned grid and stated observable-matched mock extension, a W_{low} -calibrated representative can be identified, whereas pointwise peak-height intervals are not certified for the tested BG-style uncertainty law. Thus Euclidean compatibility is a necessary consistency check, but not a sufficient adequacy criterion for spectral uncertainty claims.

I. INTRODUCTION

Lattice calculations give Euclidean correlators, whereas many real-time observables are encoded in spectral functions. In the channels considered below the forward problem has the form

$$G(\tau) = \int_0^\infty d\omega K(\tau, \omega) \rho(\omega), \quad (1)$$

with a known kernel. Transport is a canonical example: Kubo relations connect viscosities, conductivities, and diffusion coefficients to the low-frequency behavior of spectral functions [1–8]. The inverse problem is ill conditioned because the kernel smooths the spectrum, the number of Euclidean time slices is small, and the data are noisy and correlated. This has motivated maximum entropy methods, Bayesian reconstruction, Backus–Gilbert estimators, stochastic analytic continuation, Gaussian-process and spectral-density methods, and neural-network approaches [9–25].

This paper addresses a different question from the choice of central spectral estimator. A band obtained from an entropy-regularized local Gaussian approximation, a resolution-kernel construction, a bootstrap ensemble, a learned conditional sampler, or another uncertainty mechanism need not have the same repeated-experiment meaning [26–30]. A visually plausible central spectrum, a small Euclidean residual, or a spread over ansatz choices does not by itself establish coverage of a nominal interval for a specified spectral functional. Nevertheless, physical conclusions are often drawn from precisely such bands:

whether a peak has moved, whether an amplitude is resolved, or whether a low-frequency sector is constrained enough to motivate a transport statement. The operational question is therefore: under a specified Euclidean-admissible data-generating process, does a nominal interval contain the true value of the physical summary with the advertised frequency?

The answer is not expected to be universal because the Euclidean kernel does not constrain all spectral directions equally. We use “functional identifiability” in an operational sense: the extent to which changes in a functional $T[\rho]$ produce distinguishable changes in Euclidean correlators under the stated covariance and admissibility assumptions. Moving a dominant peak usually changes the correlator coherently over many Euclidean times. By contrast, an infrared integral, a local peak height, or a narrow shape deformation can be partially hidden by threshold motion, broadening, redistribution among nearby bins, positivity constraints, normalization constraints, or compensation against higher-frequency strength. Thus an interval that is calibrated for ω_{peak} need not be calibrated for

$$W_{\text{low}}(\omega_c) = \int_0^{\omega_c} \rho(\omega) d\omega, \quad (2)$$

or for ρ_{peak} . The calibration problem is therefore functional dependent: Euclidean compatibility of a central reconstruction is necessary, but it does not imply calibrated uncertainty for every physical spectral functional.

This interpretation is asymmetric. A successful mock calibration does not prove that the reconstructed spectrum is the QCD spectral function, because the mock ensemble is only a specified extension of the inverse problem. A failure is nevertheless informative: if a reported uncertainty law cannot cover a target functional even in a Euclidean-compatible challenge ensemble, then that re-

* haozhengli2002@stu.pku.edu.cn

port should not be used to support the corresponding physical claim without additional assumptions. The calibration test is therefore a conditional adequacy test for uncertainty claims, not a probability assignment to nature.

The purpose of this work is to turn the reliability of a reported spectral interval into a falsifiable, target-wise statement. The procedure constructs a controlled mock ensemble by generating non-negative spectra, forwarding them through the Euclidean kernel, checking clean-correlator admissibility diagnostics, and adding controlled noise. A reconstruction method enters through the uncertainty law, sample ensemble, or interval construction it reports for specified summaries. The same empirical coverage, simulation-based calibration (SBC), physical diagnostics, and stress tests are then applied to these reported uncertainty claims [31–33].

Existing comparisons of spectral reconstructions often examine central spectra, posterior or bootstrap spreads, resolution widths, or ansatz variations. These diagnostics are useful, but they do not by themselves determine whether a nominal interval for a specified functional $T[\rho]$ has the advertised repeated-experiment coverage under a Euclidean-admissible data-generating process. The proposed calibration test is therefore complementary to, rather than a replacement for, channel-specific spectral reconstruction.

This distinction is especially important for Backus–Gilbert-type constructions. Modern BG and BG-related Gaussian-process formulations naturally define resolution-smearred spectral densities or spectral densities under algorithm-dependent smearing kernels, and the smearing target should be specified before interpreting the resulting uncertainty [17–19]. The local peak-height tests below are therefore deliberately stringent diagnostics of pointwise spectral-feature claims. They are not statements that a BG method should be judged primarily by an unsmearred peak height.

We first use a controlled Euclidean-admissible benchmark to expose summary-dependent calibration with four specified uncertainty reports: a score-based sampler, MEM-based and BR-based local uncertainty reports, and a BG-style linear-Gaussian report. The purpose is not to rank the corresponding method families, but to run a closure test of the adequacy procedure and to show that heterogeneous uncertainty reports can be tested by the same target-wise criterion. We then apply the same logic to a real finite-temperature shear correlator. A χ^2 scan first identifies fixed BG-style reconstruction settings that satisfy Euclidean compatibility. Inside this compatible family, mock calibration is used to select and interpret uncertainty reports for W_{low} , and the same scan is used to test whether the corresponding report can support pointwise peak-height claims. The shear example illustrates the central distinction: Euclidean compatibility is necessary, but it is neither an uncertainty-calibration criterion nor a functional-adequacy criterion.

The mock ensemble is not a QCD prior; all calibration

statements are conditional on the chosen spectral family, kernel, covariance model, target functional, grid, and reconstruction setting. It is a controlled mock ensemble, parallel to lattice data in the limited but essential sense that spectra are non-negative, clean correlators are images of those spectra under the chosen kernel, and the correlators satisfy explicit Euclidean structural diagnostics. At zero temperature we use complete-monotonicity-type and positive-semidefinite diagnostics motivated by the Laplace representation of a non-negative measure [34–37]. At finite temperature we use bosonic reflection symmetry and thermal positivity diagnostics appropriate to the thermal kernel [38, 39].

II. PROTOCOL

For each mock spectrum, the known value $T[\rho_{\text{true}}]$ and the reported interval $I_\alpha(T)$ define a direct coverage test. The role of the mock ensemble is to make this repeated-experiment statement well defined under a specified kernel, covariance model, spectral family, and target functional. The controlled mock ensemble is

$$\rho_{\text{true}} \sim p_{\text{mock}}(\rho), \quad \mathbf{G}_{\text{obs}} = \mathbf{K}\rho_{\text{true}} + \epsilon, \quad \epsilon \sim \mathcal{N}(0, \Sigma), \quad (3)$$

where the weighted matrix \mathbf{K} includes the quadrature weights. The stored truth, clean correlator, noisy correlator, covariance, and grids define the calibration problem. Clean correlators define membership in the controlled mock ensemble; noisy correlators are the inputs to reconstruction. Calibration statements are therefore conditional on p_{mock} , the kernel, the grid, Σ , the selected summaries, and the reconstruction setting being tested.

To compare heterogeneous methods, we use only the uncertainty object they report. We call this interface an adapter,

$$\mathcal{A}_\lambda : (\mathbf{G}_{\text{obs}}, \tau, \omega, \Sigma, \mathcal{C}) \mapsto (U_\lambda, D_\lambda), \quad (4)$$

where λ denotes method settings and \mathcal{C} collects shared physical metadata. The uncertainty report U_λ can be a posterior sample set, a local Gaussian approximation, a linearly propagated Gaussian law, a bootstrap ensemble, or another report that can be mapped to target-summary intervals. The protocol does not require the internal philosophies of MEM, BR, BG, or a score model to be identical. It records the uncertainty claim made by each reconstruction prescription and tests that claim.

Figure 1 summarizes the operational role of this added mock-calibration branch relative to a direct real-data reconstruction.

In the main comparisons every adapter is reduced to samples $\{\rho^{(s)}\}_{s=1}^S$ and to central intervals for

$$T(\rho) \in \{\omega_{\text{peak}}, \rho_{\text{peak}}, W_{\text{low}}(3)\}, \quad \rho_{\text{peak}} = \max_k \rho_k. \quad (5)$$

The zero-temperature value $\omega_c = 3$ is a predeclared target definition. Changing ω_c changes the target and requires a new calibration test rather than an extrapolation

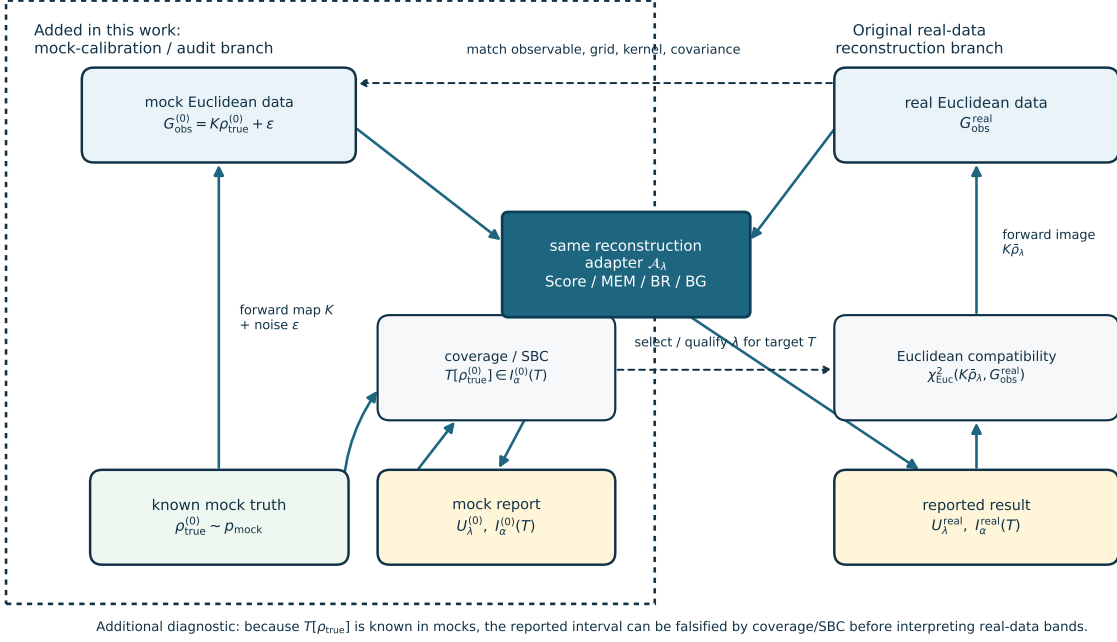


FIG. 1. Protocol workflow. The left dashed box is the added mock-calibration branch: spectra are sampled from the mock generator, forwarded through the Euclidean kernel, reconstructed with the same adapter, and compared against the known truth by coverage, SBC, and diagnostic tests. The right branch is the original real-data reconstruction path: the measured correlator is reconstructed with the same adapter and checked for Euclidean compatibility. The real-data uncertainty report is interpreted only after the corresponding mock branch has tested the target-specific interval claim.

of the old one. The empirical coverage of a nominal central interval $I_{\alpha,n}(T)$ is

$$\hat{C}_{\alpha}(T) = \frac{1}{N} \sum_{n=1}^N \mathbf{1}[T(\rho_{\text{true},n}) \in I_{\alpha,n}(T)]. \quad (6)$$

For sample-level reports we also compute SBC ranks of the true summary among the sampled summary values. Calibrated sample reports should give approximately uniform ranks [31, 32]. Pointwise spectral bands, when displayed, are interpreted only as pointwise quantile bands, not as simultaneous confidence bands over the full function.

Physical diagnostics are evaluated in addition to coverage. Central spectra are propagated back to Euclidean time, and we record normalization drift, zero-temperature monotonicity and convexity violations, finite-temperature reflection-symmetry deviations, and small positive-semidefinite matrix margins. These diagnostics check whether the reported spectra remain close to the admissible Euclidean manifold used to construct the benchmark; they do not replace coverage tests.

For mock-only demonstrations a finite candidate set Λ_{cand} is selected by a held-out calibration rule. For real data, the selection is explicitly two-step. The first re-

quirement is the Euclidean compatibility criterion,

$$\frac{\chi_{\text{Euc}}^2(\lambda)}{N_{\tau}} = \frac{1}{N_{\tau}} \left\| \Sigma^{-1/2} [K\bar{\rho}_{\lambda} - G_{\text{obs}}] \right\|_2^2 < \chi_{\text{cut}}^2, \quad (7)$$

For normalized transfer observables, G_{obs} and $K\bar{\rho}_{\lambda}$ in Eq. (7) denote the corresponding preprocessed observable and forward image, including the fixed ultraviolet convention when present. Alternatively, one can report the full χ^2 -calibration map over candidates. This criterion asks only whether the reported central spectrum is compatible with the Euclidean data under the stated error model. It does not certify an uncertainty interval.

The second layer is target-specific calibration inside the compatible family:

$$J_T(\lambda) = L_{\text{cov}}(T; \lambda) + \eta_{\text{SBC}} L_{\text{SBC}}(T; \lambda) + P_{\text{phys}}(\lambda), \quad (8)$$

$$\lambda \in \Lambda_{\chi^2},$$

where Λ_{χ^2} denotes the Euclidean-compatible candidates. The first term measures coverage error for the selected target, the second summarizes rank non-uniformity when ranks are available, and the last penalizes clear physical-diagnostic failures. Equation (8) is intentionally target dependent. A candidate can be acceptable for W_{low} and unacceptable for ρ_{peak} , or vice versa.

On real data the truth is unknown, so empirical coverage cannot be computed directly on the real correlator. The calibration information must come from an

observable-matched mock ensemble. The real-data protocol is therefore: construct a matched mock ensemble; evaluate the fixed reconstruction settings on that ensemble; require real Euclidean compatibility for the same settings; and, only inside the compatible family, use the mock calibration to choose or qualify the target-summary uncertainty report. The closure test considered here is defined by four ingredients: a known truth for $T[\rho]$, a Euclidean-admissible forward map, a stated noise model, and a reported interval from the reconstruction prescription. The test should be read as a conditional adequacy test. Passing the test means that the reported interval has not been falsified within the specified mock extension, covariance model, grid, and target definition. Failing the test means that the tested uncertainty law is not adequate for the chosen spectral functional under that extension, even if the central spectrum is Euclidean-compatible.

III. EUCLIDEAN-ADMISSIBLE BENCHMARK

The main benchmark is generated in spectral space. Spectra are mixtures of one to three positive Gaussian or log-Gaussian components, optionally thresholded, with a flexible non-negative high-frequency tail. A zeroth-moment control

$$S_0[\rho] = \int_0^\infty \rho(\omega) d\omega \quad (9)$$

keeps the global scale near a target value. In the soft-normalized family used for diversity studies the measured mean is $S_0 = 1.00003$ with standard deviation 0.00495. The effective spectral locations and widths still vary broadly across the ensemble. This construction is a physically constrained mock ensemble with controlled support, scale, and morphology. As emphasized above, its calibration statements remain conditional on the chosen spectral family, kernel, covariance, and target functional.

The clean correlator is obtained by applying the appropriate kernel before noise is added. For zero temperature we use a Laplace kernel. Clean samples are checked by discrete complete monotonicity and Hankel positive-semidefinite diagnostics. For the finite-temperature branch the thermal bosonic kernel is used, complete monotonicity is not imposed, and the clean gate instead checks midpoint reflection $G(\tau) = G(\beta - \tau)$ together with finite-dimensional positivity diagnostics. In the reported constructive ensemble the clean gates pass at essentially unit rate for both branches. The admissibility check therefore confirms that the generator lies in the intended domain; it is not a severe rejection filter that rescues pathological proposals.

The fiducial zero-temperature calibration test uses a Toeplitz covariance

$$\Sigma_{ij} = \sigma^2 \exp(-|i - j|a_\tau/\ell), \quad \sigma^2 = 10^{-5}, \quad \ell = 0.25, \quad (10)$$

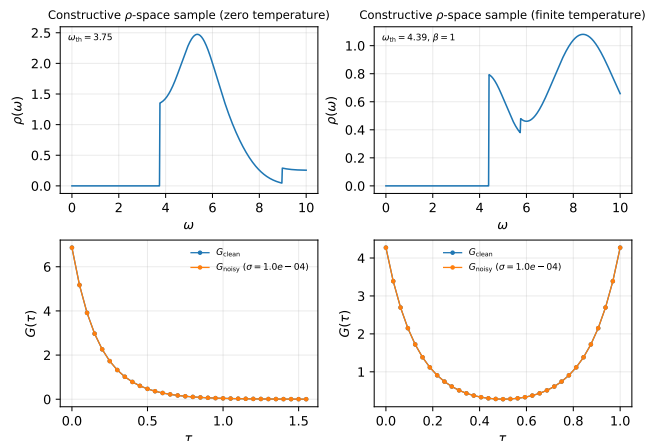


FIG. 2. Representative spectra and Euclidean correlators from the constructive benchmark. The left column illustrates the zero-temperature branch and the right column the finite-temperature branch. Clean correlators are tested by channel-appropriate admissibility diagnostics before noise is added.

with $N_\tau = 32$. The stress campaign varies N_τ , σ^2 , ℓ , the covariance supplied to inference, the spectral-family descriptors, and sampler-side constraints. Thus the mock data are not a single curve. They define a controlled Euclidean inverse problem in which Euclidean admissibility, observation noise, and spectral morphology can be changed separately.

The generator defines a controlled Euclidean inverse problem with known truth, explicit spectral positivity, channel-dependent clean-correlator admissibility, tunable covariance structure, and recorded morphology labels. These ingredients provide the setting in which a repeated-experiment statement about an uncertainty band can be tested. The limitations of the benchmark are also explicit. It contains positivity, thresholds, a simple normalization control, and generic ultraviolet variation, but it does not encode the detailed physics of every QCD channel. A transport analysis would ultimately need constraints on $\rho(\omega)/\omega$ near $\omega = 0$, perturbative or OPE-inspired ultraviolet behavior, known sum rules, contact or subtraction conventions, and the full lattice covariance.

IV. CALIBRATION RESULTS

The purpose of this generic benchmark is methodological: it is a closure test of the calibration procedure and a demonstration that different spectral summaries can have different operational identifiability. The physics-facing adequacy test is the shear application in Sec. V.

The selected representatives are a conditional score sampler, a MEM-based adapter, a BR-based adapter, and a Backus–Gilbert-type adapter. Throughout this section, the reported coverages quantify the uncertainty laws produced by these specified adapters, not the intrinsic

TABLE I. Fiducial 95% empirical coverage at $(N_\tau, \sigma^2, \ell) = (32, 10^{-5}, 0.25)$. All representatives use the same held-out cases, summaries, sample budget, and central-interval construction. Nominal coverage would be 0.95. These values quantify the reported uncertainty laws generated by the specified adapters, not the intrinsic resolving power of the corresponding reconstruction families.

Method	ω_{peak}	ρ_{peak}	W_{low}
Score	0.824	0.633	0.312
MEM-based	0.539	0.000	0.066
BG-type	0.887	0.762	0.125
BR-based	0.793	0.457	0.023

sic resolving power of the corresponding reconstruction families. The score model is trained on accepted mock spectra and noisy correlators and sampled with a warm-prior initialization and sampler-side physical projection. MEM and BR use entropy-regularized optima lifted by local or evidence-weighted Laplace-type uncertainty. BG uses the Gaussian law induced by linear propagation through the BG reconstruction matrix. These adapters are described in Appendix C. The following comparison concerns these reported uncertainty laws only; it is not a ranking of reconstruction philosophies or of all accepted MEM, BR, and BG implementations.

Table I gives the numerical anchor. At the fiducial point, the score representative gives 95% coverages 0.824, 0.633, and 0.312 for ω_{peak} , ρ_{peak} , and W_{low} , respectively. BG gives good peak-position coverage, 0.887, but only 0.125 for W_{low} . MEM-based and BR-based local uncertainty reports show that smooth entropy-regularized central spectra do not by themselves imply calibrated intervals. With $N = 256$ cases, the binomial standard error is only a few percent, so the infrared deficits are not Monte Carlo fluctuations.

The rank diagnostics carry the same message for the sample-producing score representative. Table II lists the two-sided Kolmogorov–Smirnov statistic of the SBC rank distribution at the fiducial and hard operating points. The low-frequency ranks are far more nonuniform than the peak-location ranks, even when the 95% coverage alone is already visibly low. Thus the infrared problem is not only a tail-interval effect; the full sampled distribution is displaced relative to the mock truth.

Table III gives a nearby-cutoff rescan for the low-frequency weight. The same fixed representatives are evaluated at $\omega_c = 2, 3, 4$, without retraining or retuning. The numerical severity changes with the cutoff, but nominal 95% coverage is not restored in either the fiducial or hard setting. Across the entries in Table III, the largest 95% coverage is only 0.453, and most values are much smaller. The corresponding rank nonuniformity remains large: the D_{KS} values range from 0.349 to 0.984 over the same rescan. This rules out the interpretation that the $W_{\text{low}}(3)$ undercoverage is an accident of the single predeclared cutoff.

TABLE II. Representative SBC rank diagnostics for the selected score-based uncertainty report. The columns D_{KS} are two-sided Kolmogorov–Smirnov distances of the rank distribution from uniformity. The same cases also give the raw 95% coverages shown in the last three columns.

Setting	D_{KS}			$C_{0.95}$		
	ω_{peak}	ρ_{peak}	W_{low}	ω_{peak}	ρ_{peak}	W_{low}
P_{mid}	0.149	0.280	0.652	0.824	0.633	0.312
P_{hard}	0.219	0.340	0.672	0.555	0.441	0.207

The range summary in Fig. 3 supports the same conclusion while leaving the dense cell-by-cell stress matrix to Appendix E. For the score representative, the 95% coverage of ω_{peak} ranges from 0.551 to 0.984, whereas the corresponding coverage of W_{low} ranges only from 0.207 to 0.434. The specified classical adapters fail differently: the BG-type uncertainty report is closer to nominal for peak localization, while the local MEM and BR uncertainty lifts are often much too narrow for peak height and infrared weight. The full matrices and the original heat-map visualization are collected in Appendix E.

The benchmark reveals a hierarchy of operational functional identifiability. A peak displacement changes the Euclidean correlator in a relatively coherent way. The low-frequency integral is much less localized in data space. It changes under threshold shifts, broadening, redistribution within the infrared region, and compensation against the fixed total normalization. Positivity and the S_0 projection couple the infrared region to the rest of the spectrum. Thus a method can report useful uncertainty for a dominant peak position while being overconfident for an infrared proxy under the stated mock ensemble and covariance model.

Covariance and family shifts further show that calibration is conditional. If data are generated with the fiducial Toeplitz covariance but inference is supplied with $\Sigma' = a\Sigma$, the score representative loses coverage for both peak and infrared summaries. Supplying only $\text{diag}(\Sigma)$ is less damaging for the score model in the tested setting, but it can be more harmful for MEM and BR, whose likelihoods and local uncertainty approximations depend directly on the covariance geometry. The calibration test therefore turns covariance assumptions into explicit inputs rather than implicit choices.

The out-of-family test is the sharpest stress test. Training and selection are performed on a family with lower thresholds, fewer peaks, and steeper tails, and the calibration test is moved to spectra with higher thresholds, more peaks, and softer tails. At the fiducial point the threshold-only shift changes the score coverage for W_{low} from $(C_{0.68}, C_{0.95}) = (0.777, 0.840)$ in family to $(0.098, 0.137)$ out of family. This identifies threshold support as a leading variable controlling the infrared summary in the present benchmark. Peak multiplicity alone is not the dominant cause of the observed failure.

Several ablations rule out simpler explanations. Re-

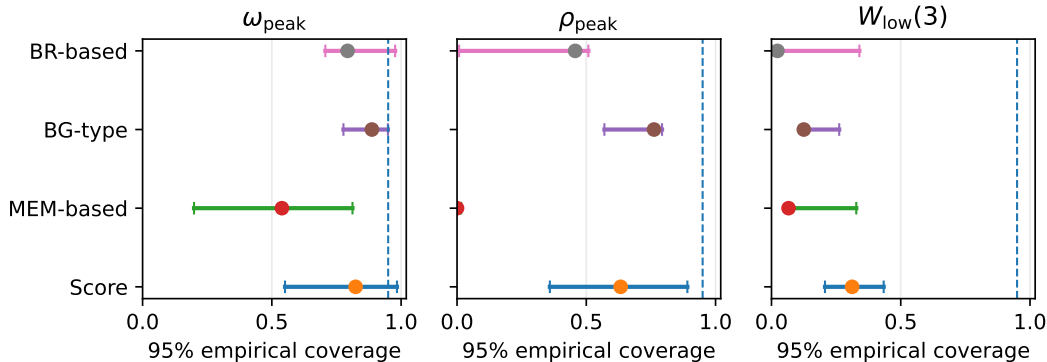


FIG. 3. Summary of the primary calibration stress matrix over the 3×3 grid in (N_τ, σ^2) at fixed Toeplitz correlation length $\ell = 0.25$. Each horizontal interval shows the range of 95% empirical coverage over the stress grid, the marker shows the fiducial point $(N_\tau, \sigma^2, \ell) = (32, 10^{-5}, 0.25)$, and the dashed vertical line marks nominal 0.95 coverage. Peak position is the most calibratable summary, whereas the low-frequency weight remains strongly undercovered across methods.

TABLE III. Cutoff-rescan sanity check for the low-frequency weight. The entries are 95% empirical coverages for $W_{\text{low}}(\omega_c) = \int_0^{\omega_c} \rho(\omega) d\omega$, evaluated with the same fixed representatives selected for the original $\omega_c = 3$ audit. No retraining or retuning is performed. The two settings are the fiducial $P_{\text{mid}} = (N_\tau, \sigma^2, \ell) = (32, 10^{-5}, 0.25)$ and the harder $P_{\text{hard}} = (16, 10^{-4}, 0.25)$.

Method	P_{mid}		P_{hard}			
	$\omega_c = 2$	$\omega_c = 3$	$\omega_c = 4$	$\omega_c = 2$	$\omega_c = 3$	$\omega_c = 4$
Score	0.125	0.312	0.422	0.129	0.207	0.359
MEM-based	0.074	0.066	0.176	0.117	0.262	0.453
BG-type	0.063	0.125	0.336	0.113	0.207	0.293
BR-based	0.000	0.023	0.000	0.016	0.059	0.078

moving individual sampler-side Euclidean filters changes the selected score representative only mildly once the training spectra already satisfy the clean gates. Dropping the S_0 control produces visible normalization drift but does not restore infrared calibration. Increasing an effective posterior temperature widens some intervals, but W_{low} remains far below nominal coverage and peak localization degrades. The low-frequency failure is therefore not a plotting artifact or a single tuning mistake. It is a weakly identifiable direction exposed by the mock calibration test.

All zero-temperature statements about W_{low} use the predeclared cutoff $\omega_c = 3$ in the working units of the archived runs. The conclusion is not that every possible infrared functional has the same numerical coverage. It is that the tested uncertainty reports are not certified for this fixed transport-motivated infrared summary. The nearby-cutoff rescan in Table III treats $\omega_c = 2$ and 4 as new summaries rather than extrapolating from $\omega_c = 3$. The result strengthens the infrared conclusion: while the numerical coverage is cutoff dependent, the tested reports remain far below nominal coverage throughout this local rescan. This keeps the infrared claim falsifiable and avoids turning one calibrated target into an unstated continuum of targets. A channel-specific transport analysis should repeat the same audit for the corresponding dimensionless ω/T target or Kubo-limit functional.

V. REAL-DATA SHEAR TRANSFER: W_{low} CALIBRATION AND PEAK-HEIGHT FAILURE

We now apply the same calibration test to a real finite-temperature shear correlator. We use the released shear correlator as a real-data transfer test of functional adequacy. The target is the reliability of reported spectral-summary intervals under the stated observable matching and covariance assumptions, rather than a determination of η/s or a reproduction of the full source-analysis transport extraction. The test has two requirements. First, the reported central spectra must be Euclidean-compatible with the released correlator. Second, within that compatible family, the uncertainty budgets for a chosen target summary are selected or rejected using calibration measured on an observable-matched mock ensemble. This section therefore asks which physical claims are supported by the tested BG-style uncertainty law once Euclidean compatibility has already been imposed.

The observable-matched benchmark follows the normalized shear channel of Ref. [8]. Synthetic finite-temperature spectra are propagated with the bosonic kernel, sliced to the retained τT points, and normalized to

$$y(\tau) = \frac{G(\tau)}{G_{\text{norm}}(\tau)}. \quad (11)$$

The finite-temperature target tested below is not the

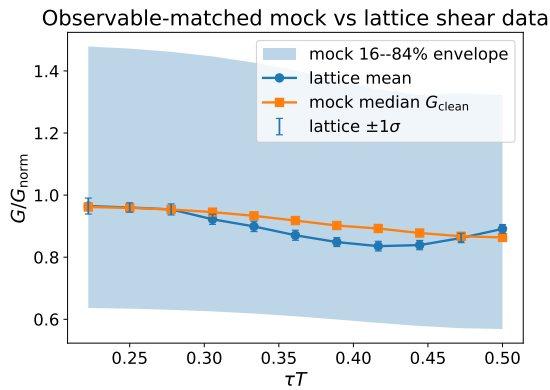


FIG. 4. Observable-matched finite-temperature shear benchmark. The released normalized shear correlator is compared with the mock median and 16–84% envelope on the retained τT support. This checks scale and support for the transfer environment; the calibration statement remains conditional on the observable-matched mock ensemble.

zero-temperature $W_{\text{low}}(3)$ of Sec. IV. We define

$$W_{\text{low}}^{\text{sh}}(\Omega_c) = \int_0^{\Omega_c} \rho_{\text{sh}}^{\text{work}}(\Omega) d\Omega, \quad \Omega = \omega/T, \quad \Omega_c = 3, \quad (12)$$

where $\rho_{\text{sh}}^{\text{work}}$ is the spectrum in the normalized-observable, fixed-ultraviolet convention of the transfer setup. This infrared weight is used to test an uncertainty report in the working normalized convention; it is not a Kubo-limit estimator of the shear viscosity.

The published pointwise errors are used as a heteroscedastic diagonal covariance for this normalized observable. This diagonal approximation is a limitation: the χ^2 values below are standardized residual diagnostics under the working error model, not full goodness-of-fit probabilities based on a complete covariance matrix.

Figure 4 shows that the real shear observable lies on the same scale as the observable-matched mock benchmark. As a separate feasibility check, a direct non-negative Euclidean fit under the same observable preprocessing, diagonal errors, finite-temperature kernel, working frequency grid, and fixed ultraviolet convention gives

$$\chi_{\text{data}}^2/N_\tau = 0.855, \quad \max_i |z_i| = 1.776, \quad (13)$$

for the 11 retained shear points. The retained real correlator is therefore not outside the working forward setup. The remaining question is whether the reported uncertainty interval is calibrated for the chosen spectral summary.

We evaluate 8001 fixed BG-style reconstruction settings and compare their Euclidean residuals with their mock-calibration diagnostics. The smallest Euclidean mismatch is

$$\min_\lambda \chi_{\text{Euc}}^2(\lambda)/N_\tau = 1.267, \quad (14)$$

for reconstruction setting 07942. The scan contains 119 reconstruction settings with $\chi^2/N_\tau < 1.5$, 154 with

$\chi^2/N_\tau < 2$, and 160 with $\chi^2/N_\tau < 4$. This establishes that the real shear correlator admits a non-trivial Euclidean-compatible BG-style family within the scanned set of reconstruction settings.

For the map below we use

$$J_W = \max_{\alpha \in \{0.68, 0.95\}} \left| \widehat{C}_\alpha(W_{\text{low}}) - \alpha \right| + 0.2D_{\text{KS}}(W_{\text{low}}), \quad (15)$$

with no additional physical-diagnostic penalty after invalid settings have been removed. Thus Fig. 5 displays the two validation requirements directly: real-data Euclidean compatibility on the horizontal axis and matched-mock target calibration on the vertical axis.

Figure 5 separates two logically distinct requirements: agreement with the Euclidean correlator and calibration of the target-summary interval. The compatible reconstruction settings do not have identical mock-calibration behavior for W_{low} . Some reports fit the real Euclidean correlator very well but are overconservative for W_{low} ; others have similar real-data χ^2 but a smaller target-specific calibration loss. A pure χ^2 choice would therefore answer only whether the central spectrum can explain the Euclidean data. It would not answer whether the W_{low} interval has the intended repeated-experiment interpretation in the matched mock ensemble.

Table V and Fig. 6 give the uncertainty-budget outcome and the per-time Euclidean residual check. The three representatives have nearly the same W_{low} central value, around 6.3–6.5 in the working units, and all have $\chi^2/N_\tau \simeq 1.3$ under the archived scalar compatibility criterion. Their 68% widths, however, range from 3.11 to 7.15. The selected reports therefore give similar real-data W_{low} medians but substantially different interval widths, showing that the uncertainty claim is not determined by the Euclidean central fit alone. The χ^2 -best setting overcovers the target in the matched mock calibration. The W_{low} -calibrated representative has $C_{0.68} = 0.668$ and $C_{0.95} = 0.961$, close to nominal at the finite calibration size, while remaining Euclidean-compatible on the real correlator. The forward residuals in Fig. 6 show that this compatibility is not produced by hiding a single large time-slice discrepancy: for the displayed sample-mean central spectra, all retained residuals are at about the two-standard-deviation level or smaller. Among reconstruction settings with $\chi^2/N_\tau < 4$, the selected report is one representative of the minimum- J_W equivalence class at the finite mock-sample resolution. We therefore use it as the calibration-selected W_{low} representative within the scanned grid and stated mock calibration, not as a claim of globally optimal uncertainty quantification.

The peak-height diagnostic gives the sharper adequacy test for local spectral structure. In the low- χ^2 representatives of Table V, the peak-height coverages are $C_{0.68}^{\text{pp}} = C_{0.95}^{\text{pp}} = 0$. The full scan in Fig. 5 and Table VI shows that this is not a consequence of choosing three unlucky examples: throughout the Euclidean-compatible region $\chi^2/N_\tau < 4$, all 160 BG-style reports have $C_{0.95}^{\text{pp}} = 0$ in the observable-matched mock cali-

TABLE IV. Matching choices for the finite-temperature shear transfer. The comparison is at the level of the reported uncertainty law for the Euclidean observable, rather than a full reproduction of the source shear-viscosity extraction.

Ingredient	Source analysis	Present calibration test
Observable	normalized shear correlator	$y(\tau) = G/G_{\text{norm}}$
Time support	retained continuum points	11 shear points
Errors	pointwise errors	diagonal heteroscedastic Σ
Reconstruction class	resolution cross-check	fixed BG-style linear-Gaussian reports
Not matched	transport systematics	full covariance, sum rules, continuum/flow-time systematics, full IR/UV ansatz scans

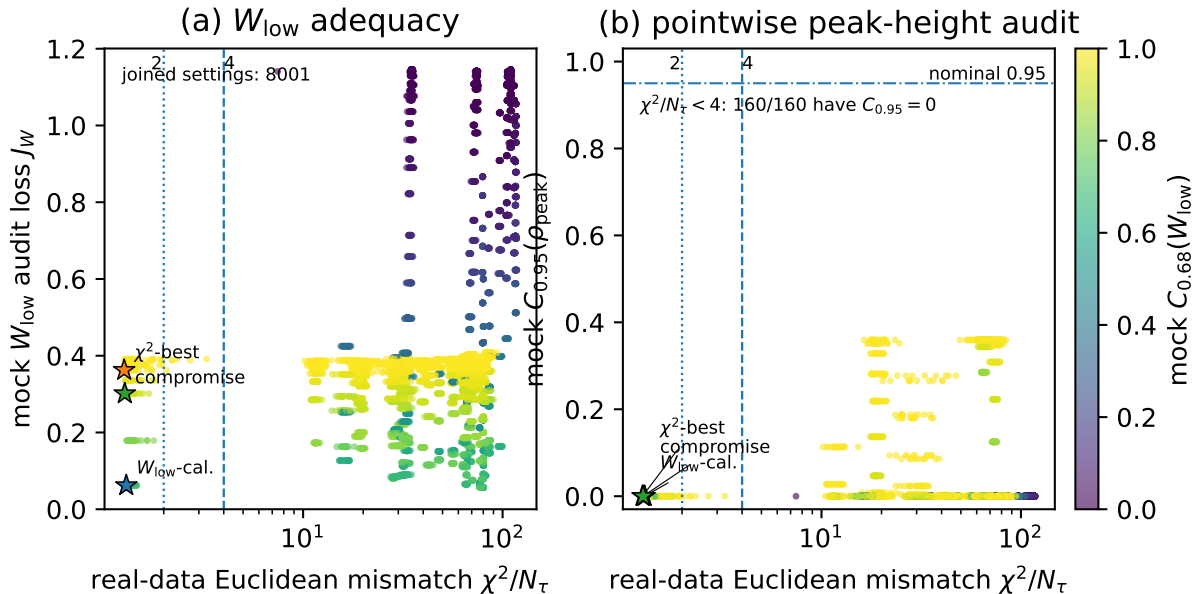


FIG. 5. Euclidean compatibility versus target-wise calibration for the 8001 fixed BG-style shear reconstruction settings. Left: the W_{low} -calibration loss J_W in Eq. (15), colored by the mock 68% coverage for W_{low} . Right: the mock 95% coverage for the pointwise peak-height target ρ_{peak} , colored by the same W_{low} coverage. The dashed and dotted vertical lines indicate $\chi^2/N_\tau = 4$ and 2, respectively, the horizontal reference line in the right panel marks nominal 0.95 coverage, and stars mark the three representative reports in Table V. In the Euclidean-compatible region, the scan contains calibrated or near-calibrated W_{low} representatives but no certified pointwise peak-height intervals for the tested BG-style uncertainty law. Since the $\chi^2/N_\tau < 2$ and $\chi^2/N_\tau < 1.5$ subsets are contained in the displayed $\chi^2/N_\tau < 4$ region, the peak-height failure persists under stricter compatibility cuts.

bration, and the same statement holds for the stricter $\chi^2/N_\tau < 2$ and $\chi^2/N_\tau < 1.5$ cuts. With 256 mock correlators, zero 95% coverage is far outside a finite-binomial fluctuation around nominal coverage, for which $\sqrt{0.95(1-0.95)}/256 = 0.014$. Thus the tested BG-style linear-Gaussian uncertainty law can describe the released shear correlator and can identify a W_{low} -calibrated representative within the scanned grid, but it does not support calibrated claims about the pointwise peak height. This result is not a theorem about all Backus–Gilbert constructions. It is a conditional rejection of the present uncertainty report for a local spectral functional under the stated observable-matched mock extension.

This is also consistent with the resolution-based nature of BG-type methods. The pointwise peak height is a stringent local diagnostic; a resolution-matched smeared peak amplitude would be a less local target and should be audited separately. The present result therefore con-

strains local peak-height claims made from this uncertainty law, rather than the use of BG-type methods for smeared spectral quantities.

The existence of a W_{low} -calibrated low- χ^2 representative in the shear example does not contradict the generic zero-temperature undercoverage result of Sec. IV. The two calibration tests use different mock ensembles, target conventions, and scanned reconstruction settings. This comparison shows that W_{low} calibration is conditional and must be tested in the target environment.

The shear example demonstrates that a reconstruction can be Euclidean-compatible while its interval for a chosen spectral summary is miscalibrated or uncertified. The shear correlator is feasible under the working forward setup, a sizable BG-style family satisfies the χ^2 compatibility criterion, and the mock-calibration test identifies a W_{low} -calibrated representative within the scanned grid that a pure χ^2 rule would not select. At the same time,

TABLE V. Representative BG-style shear reports inside the low- χ^2 family. The real-data W_{low} columns are computed from the fixed report applied to the released shear correlator. The W_{low} diagnostics $C_{0.68}$, $C_{0.95}$, and D_{KS} come from the observable-matched mock calibration. The final two columns show the peak-height target conflict: the same report family is not certified for ρ_{peak} .

Role	ID	χ^2/N_τ	W_{low} median	68% width	$C_{0.68}^W$	$C_{0.95}^W$	D_{KS}^W	$C_{0.68}^{\rho p}$	$C_{0.95}^{\rho p}$
W_{low} -calibration	07802	1.298	6.295	3.114	0.668	0.961	0.250	0.000	0.000
χ^2 -best	07942	1.267	6.345	7.155	0.980	1.000	0.310	0.000	0.000
compromise	07812	1.276	6.474	5.141	0.926	1.000	0.278	0.000	0.000

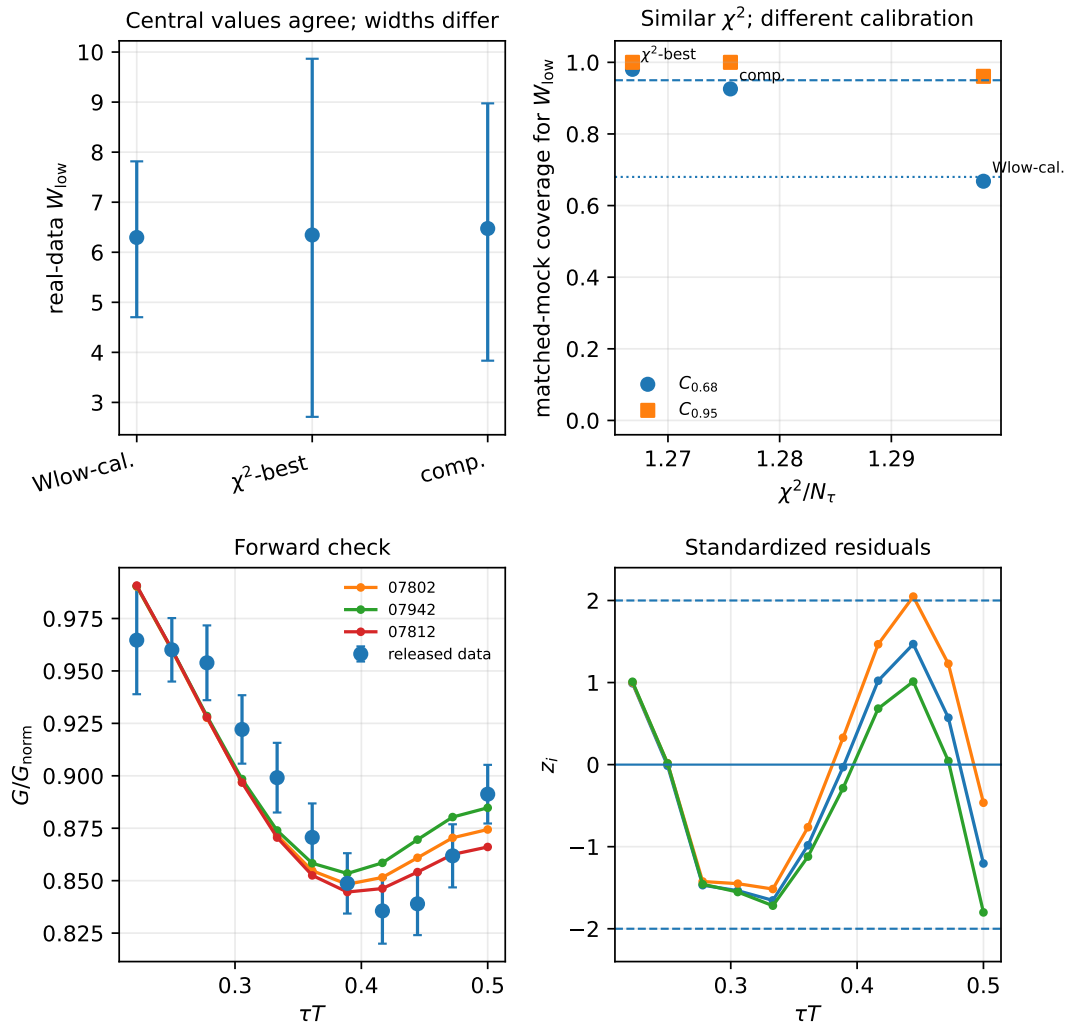


FIG. 6. Supporting checks for the three low- χ^2 shear reports. The upper-left panel shows real-data W_{low} medians and 68% intervals, and the upper-right panel shows the matched-mock coverages for the same reports. The central values are similar, while the widths differ by more than a factor of two; the χ^2 -best report is Euclidean-compatible but overcovers W_{low} , whereas the W_{low} -calibration representative is closer to nominal within the finite scanned grid. The lower panels give the per-time Euclidean forward check for the same reports: released normalized shear data and sample-mean forward images on the left, and standardized residuals $z_i = (y_{\text{model},i} - y_{\text{data},i})/\sigma_i$ on the right. Under this sample-mean central-curve convention the recomputed values are $\chi^2/N_\tau = 1.289, 1.472, \text{ and } 1.326$ for 07802, 07942, and 07812, respectively, with $\max_i |z_i| \leq 2.05$.

the same low- χ^2 family fails the pointwise peak-height audit. Therefore χ^2 is a consistency requirement on the forward correlator, not a calibration criterion for spectral uncertainty or local spectral structure. The transfer test remains conditional on the diagonal covariance,

the observable-matched mock ensemble, and the absence of full transport systematics such as known sum rules, continuum and flow-time systematics, full IR/UV ansatz scans, and a Kubo-limit target.

TABLE VI. Peak-height failure under progressively stricter Euclidean-compatibility cuts. For each cut, every retained BG-style report has zero mock coverage for the pointwise peak-height interval. The calibration size is 256 mock correlators.

Cut on χ^2/N_τ	Reports	$C_{0.68}^{pp}$ range	$C_{0.95}^{pp}$ range
< 1.5	119	0–0	0–0
< 2	154	0–0	0–0
< 4	160	0–0	0–0

VI. CONCLUSION

We have formulated a conditional model-adequacy test for spectral uncertainty claims in lattice QCD. The central question is whether a nominal interval has the advertised repeated-experiment meaning for the physical summary being interpreted. The protocol is the operational realization of this question: it constructs a Euclidean-admissible mock ensemble with known truth, maps heterogeneous reconstruction outputs to reported uncertainty laws, and tests empirical coverage, SBC ranks, physical diagnostics, and stress stability. The test is intentionally asymmetric: passing does not prove QCD truth, but failing invalidates the tested uncertainty claim for the chosen functional within the stated mock extension.

The generic benchmark shows that calibration follows a hierarchy of operational functional identifiability. In the tested mock ensemble, peak locations are substantially easier to calibrate than peak heights or the low-frequency weight $W_{\text{low}}(3)$. This hierarchy has a natural inverse-problem interpretation: coherent peak shifts are more visible in Euclidean time than local amplitudes or infrared redistributions that can be compensated elsewhere in the spectrum. The result should be read conditionally, not as a universal ranking of reconstruction families.

The shear transfer gives the physics-facing adequacy test. The released shear correlator admits a nontrivial low- χ^2 BG-style family, so the tested reports are not rejected by Euclidean compatibility alone. Within the scanned grid and stated observable-matched mock extension, the W_{low} uncertainty budget is target dependent and a calibrated representative can be identified by mock calibration. However, the same Euclidean-compatible reports do not certify the pointwise peak-height summary. This identifies a limitation of the tested BG-style uncertainty law for local spectral-feature claims: good Euclidean compatibility does not imply that all spectral functionals are reliably resolved.

The test is portable because it acts on the reported uncertainty claim itself. It requires only that the reconstruction output can be mapped to intervals or samples for $T[\rho]$, independent of the internal reconstruction philosophy. Future applications should replace the generic mock families by channel-specific benchmarks, in-

clude full covariance matrices and known sum rules, audit Kubo-limit and resolution-matched smeared targets directly, and extend the selection to multi-correlator and continuum-limit settings. Spectral uncertainty bands should be validated for the physical summaries they are used to support.

DATA AND CODE AVAILABILITY

A reproducibility package supporting this manuscript has been archived on Zenodo under DOI 10.5281/zenodo.20606367. It contains the dataset-generation scripts, adapter definitions, coverage-evaluation entry points, reconstruction-grid metadata, plotting scripts, and the joined shear χ^2 -calibration table used in Fig. 5 and Table VI. The real-shear calibration test uses the released flow-extrapolated shear correlator of Ref. [8]. The ancillary package includes the archived BG-style χ^2 scan, mock-calibration summaries, peak-height coverage columns, selected real-data W_{low} summaries, and per-time residual diagnostics needed to reproduce Figs. 5 and 6.

ACKNOWLEDGMENTS

The author thanks members of the Center for High Energy Physics, Peking University, for helpful discussions. The numerical experiments were carried out using local computing resources. Generative AI tools were used solely to assist with language editing for grammar, wording, and readability. All scientific ideas, data generation, calculations, figures, references, and final interpretations were produced and verified by the author.

Appendix A: Kernels and admissibility diagnostics

This appendix records the Euclidean kernels and the clean-correlator diagnostics used to define the benchmark. These checks are practical finite-dimensional diagnostics, not a complete axiomatization of QCD correlators.

At zero temperature we use

$$G(\tau) = \int_0^\infty d\omega e^{-\omega\tau} \rho(\omega), \quad (\text{A1})$$

with $\rho(\omega) \geq 0$ in the benchmark channels. On the working grid,

$$G_i = \sum_{k=1}^K w_k e^{-\omega_k \tau_i} \rho_k \equiv \sum_k \tilde{K}_{ik} \rho_k. \quad (\text{A2})$$

At finite temperature, for the bosonic transfer study,

$$K_\beta(\tau, \omega) = \frac{\cosh[\omega(\tau - \beta/2)]}{\sinh(\beta\omega/2)}, \quad (\text{A3})$$

which implies $G(\tau) = G(\beta - \tau)$.

For the zero-temperature Laplace kernel, a non-negative measure implies complete monotonicity,

$$(-1)^n \frac{d^n G(\tau)}{d\tau^n} \geq 0. \quad (\text{A4})$$

On the discrete grid we use forward differences and require

$$(-1)^n \Delta^n G_i \geq -\epsilon_n^{\text{CM}}, \quad n = 0, \dots, n_{\text{max}}, \quad (\text{A5})$$

with

$$\epsilon_n^{\text{CM}} = a_{\text{tol}} + r_{\text{tol}} \max_i |\Delta^n G_i|. \quad (\text{A6})$$

Unless otherwise stated $n_{\text{max}} = \min(10, N_\tau - 1)$. Complete monotonicity is applied to clean zero-temperature correlators and is not imposed in the thermal branch.

We also monitor finite-dimensional positive-semidefinite matrices. A Hankel matrix of depth m is

$$H_{ab} = G_{a+b}, \quad a, b = 0, \dots, m-1, \quad (\text{A7})$$

and a Toeplitz matrix is

$$T_{ab} = g_{|a-b|}. \quad (\text{A8})$$

The matrices are symmetrized before diagonalization, and we record the smallest eigenvalue. These PSD tests are diagnostics of the finite benchmark, not necessary and sufficient conditions for the full physical correlator cone.

The default clean gates are

$$\mathcal{G}_0[G] = \mathbf{1}[\text{CM}(G) \wedge \text{HankelPSD}(G)] \quad (\text{A9})$$

for zero temperature and

$$\mathcal{G}_\beta[G] = \mathbf{1}[\text{Palindrome}(G) \wedge (\text{HankelPSD}(G) \vee \text{ToeplitzPSD}(G))]. \quad (\text{A10})$$

for finite temperature. The gate is applied primarily to G_{clean} . Direct noisy-sequence tests are useful stress diagnostics but are not used to define the physical mock universe.

A projection-based correlator control route is also implemented. It alternates structured PSD or complete-monotonicity projections with a non-negative least-squares realizability check,

$$\hat{\rho} = \arg \min_{\rho_k \geq 0} \|G - \tilde{K}\rho\|_2^2, \quad r_{\text{rel}} = \frac{\|G - \tilde{K}\hat{\rho}\|_2}{\|G\|_2 + 10^{-16}}. \quad (\text{A11})$$

This route is used as a control study to distinguish Euclidean structural repair from realizability by a non-negative spectrum on the chosen grid.

TABLE VII. Validation statistics for the constructive benchmark. Gate rates refer to clean correlators. Normalization statistics are absolute residuals from $S_0^* = 1$.

Diagnostic	Zero temperature	Finite temperature
Main clean-gate rate	1.00000	1.00000
Filtered accepted set	64/64	64/64
Mean $ S_0 - S_0^* $	3.9589×10^{-3}	3.9589×10^{-3}
Median $ S_0 - S_0^* $	3.2777×10^{-3}	3.2777×10^{-3}
95th percentile $ S_0 - S_0^* $	9.6817×10^{-3}	9.6817×10^{-3}

Appendix B: Mock ensemble construction and validation

The constructive benchmark uses mixtures of Gaussian and log-Gaussian components. A Gaussian component has

$$\rho_G(\omega) = A \exp\left[-\frac{(\omega - \mu)^2}{2\sigma^2}\right], \quad (\text{B1})$$

with

$$\begin{aligned} \mu &\sim \text{Unif}(0.2\omega_{\text{max}}, 0.95\omega_{\text{max}}), \\ \sigma &\sim \text{Unif}(0.03\omega_{\text{max}}, 0.15\omega_{\text{max}}), \\ A &\sim \text{Unif}(0.3, 2.0). \end{aligned} \quad (\text{B2})$$

A log-Gaussian component has

$$\rho_{\log G}(\omega) = A \exp\left[-\frac{(\log \omega - \mu_{\log})^2}{2\sigma_{\log}^2}\right] \Theta(\omega), \quad (\text{B3})$$

with $\mu_{\log} = \log u$, $u \sim \text{Unif}(0.1\omega_{\text{max}}, 0.8\omega_{\text{max}})$, $\sigma_{\log} \sim \text{Unif}(0.2, 0.6)$, and $A \sim \text{Unif}(0.2, 1.5)$. The number of components is one, two, or three. A threshold $\omega_{\text{th}} \sim \text{Unif}(0, 0.6\omega_{\text{max}})$ masks the peak sector below threshold.

An optional non-negative tail,

$$\rho_{\text{tail}}(\omega) = c_{\text{tail}} \left(\frac{\omega}{\omega_{\text{ref}}}\right)^p \Theta(\omega - \omega_{\text{tail}}), \quad (\text{B4})$$

uses $c_{\text{tail}} \sim \text{Unif}(0, 0.5)$, $p \sim \text{Unif}(-2, 2)$, $\omega_{\text{tail}} \sim \text{Unif}(0.5\omega_{\text{max}}, 0.9\omega_{\text{max}})$, and $\omega_{\text{ref}} = \omega_{\text{max}}$. This tail is only a flexible ultraviolet tail component.

Hard normalization rescales the spectrum to a target S_0^* . The soft-alignment mode multiplies this rescaling by

$$u \sim \text{LogNormal}\left(-\frac{\sigma_u^2}{2}, \sigma_u\right), \quad \sigma_u = 0.005, \quad (\text{B5})$$

so that $\mathbb{E}[u] = 1$. In the 2000-sample soft-alignment report the mean absolute residual from $S_0^* = 1$ is 3.9589×10^{-3} , the median is 3.2777×10^{-3} , and the 95th percentile is 9.6817×10^{-3} .

A 5000-sample diversity report gives effective spectral mean 6.62997 with 5th-to-95th percentile range 4.44028 to 8.34990, effective width mean 1.64439 with range 0.88787 to 2.50641, and support-width mean 6.84110 with range 4.28571 to 9.54990. The family therefore

spans support locations, widths, and peak configurations while retaining a controlled global scale.

The projection-based correlator control route has main and realizability rates 0.99400 for the zero-temperature control and 1.00000 for the finite-temperature control in 2000-sample reports. Accepted zero-temperature samples have maximum relative NNLS residual 1.79696×10^{-9} , and finite-temperature samples have maximum residual 9.70482×10^{-9} . This route is viable but more delicate than the constructive route, so the latter is used for the main audit.

Appendix C: Reconstruction adapters

The adapters below define the uncertainty reports tested in this work. They expose each method’s reported uncertainty law in a common sample-level form without making the methods philosophically identical. The calibration results should therefore be interpreted as statements about these reported uncertainty laws, not as general theorems about MEM, BR, BG, or score-based reconstruction.

The conditional score representative is trained in scaled variables with a variance-exploding denoising score-matching objective [40–42]. For noise level σ and $\xi \sim \mathcal{N}(0, I)$,

$$\tilde{\rho}_\sigma = \tilde{\rho} + \sigma\xi, \quad s^* = -\frac{\tilde{\rho}_\sigma - \tilde{\rho}}{\sigma^2}, \quad (\text{C1})$$

and the network minimizes a weighted denoising score loss. Sampling uses a predictor–corrector discretization on a decreasing VE schedule. The selected representative uses warm-prior initialization with $(\sigma_{\min}, \sigma_{\max}, N_{\text{step}}) = (0.01, 1.0, 64)$ and shared physical projection.

The MEM adapter maximizes

$$Q(\rho; \alpha) = \alpha S(\rho, m) - \frac{1}{2} \chi^2(\rho), \quad (\text{C2})$$

with

$$S(\rho, m) = \sum_k w_k \left[\rho_k - m_k - \rho_k \log \left(\frac{\rho_k}{m_k} \right) \right] \quad (\text{C3})$$

and the usual Gaussian likelihood term. Positivity is enforced through $\rho_k = m_k \exp(y_k)$. The reported uncertainty is a stabilized Laplace or evidence-weighted local sample law around the selected solution [26]. This is the tested MEM-based uncertainty law.

The BR adapter uses the Burnier–Rothkopf functional [13],

$$S_{\text{BR}}(\rho, m) = \alpha \sum_k w_k \left[1 - \frac{\rho_k}{m_k} + \log \left(\frac{\rho_k}{m_k} \right) \right], \quad (\text{C4})$$

again in the exponential parameterization. The selected branch uses integrated- α optimization and a Laplace-type uncertainty lift. This is the tested BR-based uncertainty law.

The BG adapter constructs a linear estimator

$$\hat{\rho} = QG_{\text{obs}} \quad (\text{C5})$$

and reports the induced Gaussian law

$$q_{\text{BG}}(\rho | G_{\text{obs}}) = \mathcal{N}(QG_{\text{obs}}, Q\Sigma Q^T). \quad (\text{C6})$$

Ranks for BG are therefore calibration diagnostics of this reported linear-Gaussian law.

Failed optimizer calls, singular covariance factorizations, invalid samples, and non-finite entries are recorded in the adapter metadata. A reconstruction setting that appears calibrated only after silent case removal is not treated as a valid uncertainty report.

Appendix D: Metrics and selection

For each sampled spectrum we compute

$$\begin{aligned} \omega_{\text{peak}} &= \omega_{\arg \max_k \rho_k}, & \rho_{\text{peak}} &= \max_k \rho_k, \\ W_{\text{low}}(\omega_c) &= \sum_{\omega_k \leq \omega_c} w_k \rho_k. \end{aligned} \quad (\text{D1})$$

The main zero-temperature audit uses $\omega_c = 3$. If several bins share the maximum within numerical tolerance, the first maximum is used consistently for truth and samples.

Central intervals are empirical quantile intervals,

$$I_\alpha(T) = \left[q_{(1-\alpha)/2} \{T(\rho^{(s)})\}, q_{(1+\alpha)/2} \{T(\rho^{(s)})\} \right]. \quad (\text{D2})$$

The empirical coverage is Eq. (6), with binomial standard error

$$\text{se}[\hat{C}_\alpha] \simeq \sqrt{\frac{\hat{C}_\alpha(1 - \hat{C}_\alpha)}{N}}. \quad (\text{D3})$$

For $N = 256$, this standard error is a few percent for the coverages reported here.

SBC ranks are defined by

$$r_n(T) = \sum_{s=1}^S \mathbf{1} \left[T(\rho_n^{(s)}) < T(\rho_{\text{true}, n}) \right], \quad (\text{D4})$$

with randomized tie handling when needed. We summarize non-uniformity with a Kolmogorov–Smirnov distance after mapping ranks to $[0, 1]$. Coverage tests advertised interval frequency; SBC is sensitive to bias and mass allocation within the reported distribution.

For the generic mock demonstration, selected representatives are chosen on held-out cases by a calibration-first score,

$$J_{\text{global}}(\lambda) = L_{\text{cov}}(\lambda) + \eta_{\text{SBC}} L_{\text{SBC}}(\lambda) + P_{\text{phys}}(\lambda), \quad (\text{D5})$$

where

$$L_{\text{cov}}(\lambda) = \max_{T \in \{\omega_{\text{peak}}, \rho_{\text{peak}}, W_{\text{low}}\}} \max_{\alpha \in \{0.68, 0.95\}} |\hat{C}_\alpha(T; \lambda) - \alpha|. \quad (\text{D6})$$

TABLE VIII. Selected representatives used in the fiducial audit.

Method	Selected representative	Audited uncertainty report
Score	prior initialization, (0.01, 1.0, 64) VE schedule, bi12 checkpoint	conditional score samples with physical projection
MEM-based	SVD search, flat- S_0 default, $\alpha \in [10^{-4}, 10^7]$, 12 nodes, classic-max	stabilized Laplace/evidence-weighted local samples
BR-based	integrated- α optimization on $[10^{-3}, 10^3]$, 16 nodes, full space	BR-MAP plus integrated- α /Laplace samples
BG-type	$\lambda = 0.5$, ridge 10^{-16} , ω -stride 2, sample scale 1.25	linear-Gaussian pseudo-posterior

The maximum prevents a severe failure for one physical summary from being hidden by better behavior on another. The fixed selection budgets are 144 MEM candidates, 400 BR candidates, 432 BG candidates, and a fixed score training/sampling grid.

For real-data transfer the rule is two-layer. The first requirement is the Euclidean compatibility criterion, Eq. (7). In the shear scan we report the full map and quote counts for several thresholds rather than claiming a unique probabilistic cutoff, because only a diagonal pointwise covariance is available. The second layer is target-specific:

$$J_T(\lambda) = \max_{\alpha \in \{0.68, 0.95\}} |\widehat{C}_\alpha(T; \lambda) - \alpha| + \eta_{\text{SBC}} D_{\text{KS}}(T; \lambda) + P_{\text{phys}}(\lambda), \quad \lambda \in \Lambda_{\chi^2}. \quad (\text{D7})$$

In the displayed shear map we use $T = W_{\text{low}}$ and $\eta_{\text{SBC}} = 0.2$ for visualization of the calibration loss. Invalid configurations are removed before plotting, and no additional physical-diagnostic penalty is applied in that displayed map; equivalently, $P_{\text{phys}} = 0$ for Fig. 5. The precise numerical ranking should not be overinterpreted beyond the finite candidate set; the qualitative requirement is that Euclidean compatibility and target calibration be reported separately.

The real-data target summary has no known truth. Therefore real-data coverage is not measured on the released correlator. It is inherited from an observable-matched mock calibration with the same preprocessing, kernel, grid, and diagonal-error convention. To reduce selection bias, the candidate grid, target definition, mock-calibration summaries, and real-data χ^2 diagnostics are treated as separate validation components. The final real-data report is conditional on all of these choices, and no selected configuration is claimed to be globally optimal outside this finite grid or under a different calibration split.

Dataset splits and selection budget

The mock calibration uses disjoint roles for training, calibration, and final evaluation. Table IX records the sizes that enter the reported generic runs. The score model is the only representative that requires a training split. Classical adapters are selected on held-out mock cases using the same target summaries and are then fixed before final evaluation. The final selected-representative

numbers in the main text use the same $N = 256$ held-out cases and $S = 128$ samples per case for all adapters.

The real-shear BG-style grid contains 8001 fixed configurations. Its mock calibration is evaluated with $N = 256$ mock cases and $S = 128$ samples per case for the stored sweep. The real W_{low} intervals in Table V use 4096 samples for the three selected configurations.

Appendix E: Full stress-test tables

This appendix records the 95% coverage matrices for the primary zero-temperature stress test. The grid is

$$(N_\tau, \sigma^2) \in \{16, 32, 48\} \times \{10^{-6}, 10^{-5}, 10^{-4}\}, \quad \ell = 0.25. \quad (\text{E1})$$

The tables below are the authoritative stress-matrix record. Figure 7 shows the full heat-map visualization corresponding to the same numbers summarized in Fig. 3.

The out-of-family score calibration test decomposes the total shift into peak-count, threshold, and tail components. At the fiducial point the threshold-only shift is the leading degradation: W_{low} changes from (0.777, 0.840) to (0.098, 0.137) at the (68%, 95%) levels. At the hard point it changes from (0.449, 0.594) to (0.023, 0.066). This supports the interpretation that threshold support is the dominant domain-shift variable for the infrared weight in the present benchmark.

Appendix F: Real-data shear-grid details

The real-data demonstration uses the viscosity-specific finite-temperature transfer setup rather than the generic zero-temperature scripts. The mock source library uses

$$\beta = 1, \quad N_\tau = 37, \quad K = 1024, \quad \omega_{\text{max}} = 20, \quad (\text{F1})$$

with a fixed ultraviolet continuation used as a numerical convention in the transfer setup. The observable-matching step slices the mock correlators to the 11 retained shear τT points, recomputes the normalization correlator on the same grid, and converts to $y(\tau) = G(\tau)/G_{\text{norm}}(\tau)$. The finite-temperature W_{low} target in Eq. (12) uses the same dimensionless grid variable $\Omega = \omega/T$ and cutoff $\Omega_c = 3$. The published pointwise errors of Ref. [8] define the diagonal covariance used for the standardized residual diagnostic.

The BG-style candidate grid is generated from fixed choices of the resolution regularization λ , ridge stabilization, contact-jitter scale, oversampling factor, scale

TABLE IX. Dataset roles and evaluation budgets used in the reported audits. The detailed train/validation/test sizes refer to the mock splits used by the score model; the final selected-representative audit uses the same held-out cases for all adapters within each benchmark setting.

Stage	Size or budget	Main use
Toy score split	10000/2000/2000	score-mechanism diagnosis
Fiducial score split	40000/8000/8000	score training and validation
Adapter selection	144 MEM; 400 BR; 432 BG; fixed score grid	choose representative adapters
Final selected audit	$N = 256$, $S = 128$	coverage, SBC, physical diagnostics
Stress audit	$N = 256$, $S = 128$ unless stated otherwise	regime and family shifts
Real shear BG grid	8001 candidates; 3 real reports with 4096 samples	two-layer χ^2 -calibration test

TABLE X. 95% empirical coverage for ω_{peak} .

Setting (N_τ, σ^2)	Score	MEM-based	BG-type	BR-based
(16, 10^{-4})	0.555	0.766	0.891	0.836
(16, 10^{-5})	0.715	0.812	0.777	0.738
(16, 10^{-6})	0.973	0.781	0.934	0.773
(32, 10^{-4})	0.590	0.324	0.945	0.977
(32, 10^{-5})	0.824	0.539	0.887	0.793
(32, 10^{-6})	0.984	0.508	0.871	0.707
(48, 10^{-4})	0.551	0.270	0.887	0.969
(48, 10^{-5})	0.758	0.199	0.949	0.902
(48, 10^{-6})	0.961	0.340	0.914	0.836

TABLE XI. 95% empirical coverage for ρ_{peak} .

Setting (N_τ, σ^2)	Score	MEM-based	BG-type	BR-based
(16, 10^{-4})	0.441	0.004	0.754	0.070
(16, 10^{-5})	0.648	0.012	0.793	0.348
(16, 10^{-6})	0.891	0.004	0.684	0.008
(32, 10^{-4})	0.402	0.016	0.730	0.508
(32, 10^{-5})	0.633	0.000	0.762	0.457
(32, 10^{-6})	0.875	0.000	0.727	0.035
(48, 10^{-4})	0.359	0.008	0.688	0.438
(48, 10^{-5})	0.609	0.012	0.570	0.023
(48, 10^{-6})	0.863	0.000	0.668	0.023

parameter, and ultraviolet cutoff convention. The scan contains 8001 configurations. The real-data χ^2 records include the configuration name, seed, unregularized standardized residual norm, and χ^2/N_τ . The best entry is configuration 07942, whose file name specifies the settings $\lambda = 10^{-3}$, ridge 10^{-8} , contact jitter 10^{-14} , oversampling 1, scale 3.5, and UV cutoff 10. It has $\chi^2/N_\tau = 1.2668$.

The target-specific mock calibration is joined to the real χ^2 scan by configuration name. For each joined reconstruction setting we compute

$$J_W = \max_{\alpha \in \{0.68, 0.95\}} |\hat{C}_\alpha(W_{\text{low}}) - \alpha| + 0.2D_{\text{KS}}(W_{\text{low}}), \quad (\text{F2})$$

which is the quantity plotted in Fig. 5. No additional physical-diagnostic penalty is applied in this displayed shear-grid map after invalid settings have been removed. Within the $\chi^2/N_\tau < 4$ compatibility set, the minimum stored value of J_W is shared by 20 configurations because the finite mock sample makes the coverage entries discrete; 07802 is used as a representative member of this minimum- J_W class. The selected real-data W_{low} table is generated from stored samples for three representa-

TABLE XII. 95% empirical coverage for $W_{\text{low}} = \int_0^3 \rho(\omega) d\omega$.

Setting (N_τ, σ^2)	Score	MEM-based	BG-type	BR-based
(16, 10^{-4})	0.207	0.262	0.207	0.059
(16, 10^{-5})	0.305	0.328	0.168	0.020
(16, 10^{-6})	0.359	0.312	0.168	0.117
(32, 10^{-4})	0.258	0.148	0.152	0.000
(32, 10^{-5})	0.312	0.066	0.125	0.023
(32, 10^{-6})	0.359	0.070	0.133	0.059
(48, 10^{-4})	0.273	0.203	0.262	0.008
(48, 10^{-5})	0.387	0.168	0.230	0.199
(48, 10^{-6})	0.434	0.168	0.211	0.340

tive configurations: 07802, 07942, and 07812. Their 68% widths are 3.114, 7.155, and 5.141, respectively, while their medians are all close to 6.3–6.5 in the working units.

The direct feasibility diagnostic is separate from the candidate-grid calibration test. It solves a non-negative least-squares problem under the same preprocessing, diagonal covariance, finite-temperature kernel, working grid, and fixed ultraviolet convention,

$$\hat{\rho}_\lambda = \arg \min_{\rho_k \geq 0} \left\| \Sigma^{-1/2} (\tilde{K}\rho + g_{\text{UV}} - y) \right\|_2^2 + \lambda \|L\rho\|_2^2, \quad (\text{F3})$$

where L is a finite-difference matrix and g_{UV} denotes the fixed ultraviolet contribution. The quoted feasibility number is the unregularized data term evaluated at the fitted spectrum,

$$\frac{\chi_{\text{data}}^2}{N_\tau} = \frac{1}{N_\tau} \left\| \Sigma^{-1/2} (\tilde{K}\hat{\rho}_\lambda + g_{\text{UV}} - y) \right\|_2^2. \quad (\text{F4})$$

The best shear value is 0.855. This feasibility diagnostic is not an uncertainty report, is not used to tune the scanned BG-style candidates, and is not a transport extraction.

The release includes the joined χ^2 -calibration table, selected W_{low} summaries, the peak-height coverage columns used in Fig. 5, and per-time residual diagnostics needed to reproduce Figs. 5 and 6. For the sample-mean central spectra displayed in Fig. 6, the recomputed χ^2/N_τ values are 1.289, 1.472, and 1.326 for 07802, 07942, and 07812, with $\max_i |z_i| = 1.654, 2.048, \text{ and } 1.801$. The exact linear BG central spectra are also archived; they give $\chi^2/N_\tau = 1.372, 1.377, \text{ and } 1.372$. These per-time diagnostics are a visual compatibility check under explicit

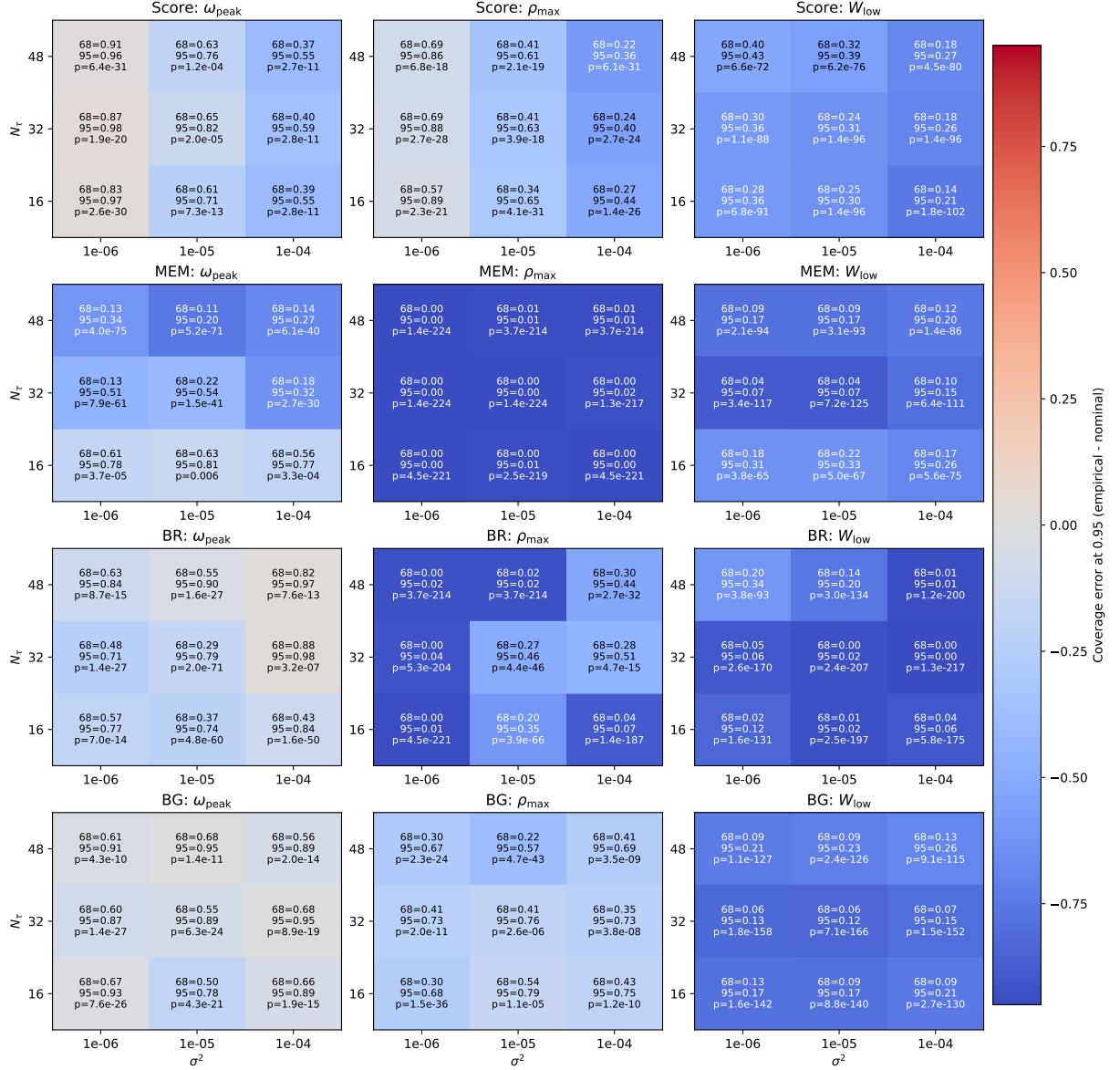


FIG. 7. Full primary calibration stress matrix over N_τ and σ^2 at fixed Toeplitz correlation length $\ell = 0.25$. Each cell reports the 68% and 95% empirical coverages and the rank-uniformity diagnostic used in the internal audit. This figure is retained as the detailed diagnostic record; the main text uses the compressed coverage-range summary in Fig. 3.

TABLE XIII. Rank nonuniformity in the nearby-cutoff rescan for $W_{\text{low}}(\omega_c)$. Entries are D_{KS} values of the SBC rank distribution for the same fixed representatives used in Table III.

Method	$\omega_c = 2$	P_{mid} $\omega_c = 3$	$\omega_c = 4$	$\omega_c = 2$	P_{hard} $\omega_c = 3$	$\omega_c = 4$
Score	0.867	0.652	0.504	0.813	0.676	0.410
MEM-based	0.824	0.742	0.653	0.758	0.574	0.349
BG-type	0.914	0.856	0.641	0.868	0.758	0.645
BR-based	0.984	0.957	0.906	0.969	0.879	0.820

central-curve conventions, while the main text uses the

archived scalar χ^2 scan for the candidate-grid compatibility criterion.

-
- [1] R. Kubo, Statistical-mechanical theory of irreversible processes. i. general theory and simple applications to magnetic and conduction problems, *Journal of the Physical Society of Japan* **12**, 570 (1957).
- [2] G. Aarts, C. Allton, J. Foley, S. Hands, and S. Kim, Spectral functions at small energies and the electrical conductivity in hot quenched lattice qcd, *Phys. Rev. Lett.* **99**, 022002 (2007).
- [3] H. B. Meyer, Calculation of the shear viscosity in su(3) gluodynamics, *Phys. Rev. D* **76**, 101701(R) (2007).
- [4] H. B. Meyer, Calculation of the bulk viscosity in su(3) gluodynamics, *Phys. Rev. Lett.* **100**, 162001 (2008).
- [5] H. B. Meyer, Transport properties of the quark-gluon plasma, *The European Physical Journal A* **47**, 86 (2011).
- [6] G. Aarts and A. Nikolaev, Electrical conductivity of the quark-gluon plasma: perspective from lattice qcd, *The European Physical Journal A* **57**, 118 (2021).
- [7] N. Y. Astrakhantsev, V. V. Braguta, and A. Y. Kotov, Temperature dependence of shear viscosity of su(3)-gluodynamics within lattice simulation, *Journal of High Energy Physics* **2017**, 101 (2017).
- [8] L. Altenkort, A. M. Eller, A. Francis, O. Kaczmarek, L. Mazur, G. D. Moore, and H.-T. Shu, Viscosity of pure-gluon qcd from the lattice, *Phys. Rev. D* **108**, 014503 (2023).
- [9] R. K. Bryan, Maximum entropy analysis of oversampled data problems, *European Biophysics Journal* **18**, 165 (1990).
- [10] M. Jarrell and J. Gubernatis, Bayesian inference and the analytic continuation of imaginary-time quantum monte carlo data, *Physics Reports* **269**, 133 (1996).
- [11] Y. Nakahara, M. Asakawa, and T. Hatsuda, Hadronic spectral functions in lattice qcd, *Phys. Rev. D* **60**, 091503(R) (1999).
- [12] M. Asakawa, Y. Nakahara, and T. Hatsuda, Maximum entropy analysis of the spectral functions in lattice qcd, *Progress in Particle and Nuclear Physics* **46**, 459 (2001).
- [13] Y. Burnier and A. Rothkopf, Bayesian approach to spectral function reconstruction for euclidean quantum field theories, *Phys. Rev. Lett.* **111**, 182003 (2013).
- [14] G. Backus and F. Gilbert, The resolving power of gross earth data, *Geophysical Journal International* **16**, 169 (1968).
- [15] A. W. Sandvik, Stochastic method for analytic continuation of quantum monte carlo data, *Phys. Rev. B* **57**, 10287 (1998).
- [16] K. S. D. Beach, Identifying the maximum entropy method as a special limit of stochastic analytic continuation (2004), arXiv:cond-mat/0403055.
- [17] M. Hansen, A. Lupo, and N. Tantalo, Extraction of spectral densities from lattice correlators, *Phys. Rev. D* **99**, 094508 (2019).
- [18] G. Bailas, S. Hashimoto, and T. Ishikawa, Reconstruction of smeared spectral functions from euclidean correlation functions, *Progress of Theoretical and Experimental Physics* **2020**, 043B07 (2020).
- [19] L. Del Debbio, A. Lupo, M. Panero, and N. Tantalo, Bayesian solution to the inverse problem and its relation to backus-gilbert methods, *The European Physical Journal C* **85**, 185 (2025).
- [20] H.-T. Ding, O. Kaczmarek, S. Mukherjee, H. Ohno, and H.-T. Shu, Stochastic reconstructions of spectral functions: Application to lattice qcd, *Phys. Rev. D* **97**, 094503 (2018).
- [21] L. Kades, J. M. Pawłowski, A. Rothkopf, M. Scherzer, J. M. Urban, S. J. Wetzel, N. Wink, and F. P. G. Ziegler, Spectral reconstruction with deep neural networks, *Phys. Rev. D* **102**, 096001 (2020).
- [22] J. Horak, J. M. Pawłowski, J. Rodríguez-Quintero, J. Turnwald, J. M. Urban, N. Wink, and S. Zafeiropoulos, Reconstructing qcd spectral functions with gaussian processes, *Phys. Rev. D* **105**, 036014 (2022).
- [23] L. Wang, S. Shi, and K. Zhou, Reconstructing spectral functions via automatic differentiation, *Phys. Rev. D* **106**, L051502 (2022).
- [24] M. Buzziotti, A. De Santis, and N. Tantalo, Teaching to extract spectral densities from lattice correlators to a broad audience of learning-machines, *The European Physical Journal C* **84**, 32 (2024).
- [25] L. Huang and S. Liang, Reconstructing lattice qcd spectral functions with stochastic pole expansion and nevanlinna analytic continuation, *Phys. Rev. D* **109**, 054508 (2024).
- [26] L. Tierney and J. B. Kadane, Accurate approximations for posterior moments and marginal densities, *Journal of the American Statistical Association* **81**, 82 (1986).
- [27] B. Efron and R. Tibshirani, *An Introduction to the Bootstrap*, 1st ed. (Chapman and Hall/CRC, 1994).
- [28] A. Rothkopf, Bayesian inference of real-time dynamics from lattice qcd, *Frontiers in Physics* **Volume 10 - 2022**, 10.3389/fphy.2022.1028995 (2022).
- [29] J. Frison, Bayesian Inference for Contemporary Lattice Quantum Field Theory, *PoS LATTICE2023*, 027 (2024).
- [30] W. Jay, Approaches to the Inverse Problem, *PoS LATTICE2024*, 002 (2025).
- [31] S. R. Cook, A. Gelman, and D. B. Rubin, Validation of software for bayesian models using posterior quantiles, *Journal of Computational and Graphical Statistics* **15**, 675 (2006).
- [32] S. Talts, M. Betancourt, D. Simpson, A. Vehtari, and A. Gelman, Validating Bayesian Inference Algorithms with Simulation-Based Calibration (2018), arXiv:1804.06788 [stat.ME].
- [33] A. M. Stuart, Inverse problems: A bayesian perspective, *Acta Numerica* **19**, 451–559 (2010).
- [34] K. Osterwalder and R. Schrader, Axioms for euclidean green's functions, *Communications in Mathematical Physics* **31**, 83 (1973).
- [35] K. Osterwalder and R. Schrader, Axioms for euclidean green's functions ii, *Communications in Mathematical Physics* **42**, 281 (1975).
- [36] F. Hausdorff, Summationsmethoden und momentfolgen. i, *Mathematische Zeitschrift* **9**, 74 (1921).
- [37] D. Widder, *The Laplace Transform*, Princeton mathematical series (Princeton University Press, 1941).
- [38] P. C. Martin and J. Schwinger, Theory of many-particle systems. i, *Phys. Rev.* **115**, 1342 (1959).
- [39] P. Lowdon, Euclidean thermal correlation functions in local qft, *Phys. Rev. D* **106**, 045028 (2022).
- [40] A. Hyvärinen, Estimation of non-normalized statistical models by score matching, *Journal of Machine Learning*

- Research **6**, 695 (2005).
- [41] P. Vincent, A connection between score matching and denoising autoencoders, *Neural Computation* **23**, 1661 (2011).
- [42] Y. Song, J. Sohl-Dickstein, D. P. Kingma, A. Kumar, S. Ermon, and B. Poole, Score-Based Generative Modeling through Stochastic Differential Equations (2020), arXiv:2011.13456 [cs.LG].